



Nickel-Copper Supported on Carbon Black Hydrogen Oxidation Catalyst Integrated into Anion-Exchange Membrane Fuel Cell

Journal:	<i>Sustainable Energy & Fuels</i>
Manuscript ID	SE-ART-06-2018-000261.R1
Article Type:	Paper
Date Submitted by the Author:	25-Jun-2018
Complete List of Authors:	Roy, Aaron; University of New Mexico, enter for Emerging Energy Technologies, Department of Chemical and Nuclear Engineering Talarposhti, Morteza; University of New Mexico, enter for Emerging Energy Technologies, Department of Chemical and Nuclear Engineering Normile, Stanley; Tufts University, Mechanical Engineering Zenyuk, Iryna; Tufts University, Mechanical Engineering de Andrade, Vincent; Argonne National Laboratory, Artyushkova, Kateryna; University of New Mexico, Chemical and Nuclear Engineering Serov, Alexey; University of New Mexico, Department of Chemical & Biological Engineering Atanassov, Plamen; University of New Mexico, Department of Chemical and Nuclear Engineering



Journal Name

ARTICLE

Nickel-Copper Supported on Carbon Black Hydrogen Oxidation Catalyst Integrated into Anion-Exchange Membrane Fuel Cell

Aaron Roy^a, Morteza R. Talarposhti^a, Stanley J. Normile^b, Iryna V. Zenyuk^b, Vincent De Andrade^c, Kateryna Artyushkova^a, Alexey Serov^a, and Plamen Atanassov^a

Received 00th
January 20xx,
Accepted 00th
January 20xx

DOI:
10.1039/x0xx0
0000x

www.rsc.org/

Abstract

This work introduces the first practical platinum group metal-free (PGM-free) electrocatalyst for hydrogen oxidation reaction (HOR) in alkaline membrane fuel cells (AMFC), based on nickel-rich Ni₉₅Cu₅-alloy nanoparticles supported on Ketjenblack (KB) family carbon blacks. The catalyst synthesis is scalable and results in expected true alloy of NiCu, which is thoroughly characterized by XRD, microscopy and XPS. Reactivity of the catalyst towards HOR is studied by cyclic voltammetry and explained in view of its composition and structure. This catalyst showed highest specific activity compared to previously reported NiCu electrocatalysts and was successfully integrated into an AMFC membrane electrode assembly (MEA) using commercially available state-of-the-art membrane and ionomer. Single MEA fuel cell tests have demonstrated power density of 350 mWcm⁻² at 80°C, which sets a technical record for a PGM-free anode in realistic operating conditions. The MEA with NiCu/KB anode catalysts layer were evaluated by *in situ* nano- and *operando* micro-X-ray computed tomography (CT) and results suggest that the nickel state in NiCu is hydrophobic in nature, where the NiCu surface may be isostructural with β-Ni(OH)₂. The hydrophobic nature of electrocatalyst allows for improved water distribution in MEA and overall fuel cell as observed with *operando* micro X-ray CT.

Broader Context: Hydrogen economy is a viable macro-economic and societal technology concept that could provide viable solution to the limitations posed by both finite fossil fuel resources and anthropogenic contributions to climate change. Current rendering of the most advanced branch of fuel cell technology, however, the one using polymer electrolyte membranes, is in its own right materials limited through its dependence on platinum group metals (PGM) as catalysts for both cathodic and anodic processes. While much work has been done to advance oxygen reduction cathode catalysts, the development of PGM-free anode catalysts is in its infancy. Hydrogen oxidation reaction (HOR) catalyst introduced through this work can pave the way to a complete PGM-free materials set and make alkaline membrane fuel cells (AMFC) a competitive alternative in more diverse, flexible energy conversion technology entirely based on Earth-abundant elements.

Introduction

Growing concerns regarding CO₂ emissions from the burning of fossil fuels, the finite abundance of fossil fuels, and the environmental impacts of the industrialized use of fossil fuels are

driving researchers to develop technologies which will enable hydrogen energy and hydrogen energy storage¹. Hydrogen fuel cells for energy conversion are therefore of considerable interest. The reduction of fuel cell costs by transitioning from proton exchange membrane fuel cells (PEMFC's) to anion exchange membrane fuel cells (AEMFC's) can be achieved due to *i*) a lower overpotential for oxygen reduction reaction (ORR) at the cathode of AEMFC's, *ii*) the ability to use Earth-abundant, platinum group metal-free (PGM-Free) catalyst materials for ORR at the cathode and also for hydrogen oxidation reaction (HOR) at the anode in AEMFC's, and *iii*) a wider range of polymer chemistry which can be

^a Department of Chemical & Biological Engineering, Center for Micro-Engineered Materials, University of New Mexico, Albuquerque, NM 87131, USA

^b Department of Mechanical Engineering, Tufts University, Medford, MA 02155

^c Advanced Photon Source, Argonne National Laboratory, Argonne, IL 60439

† Footnotes relating to the title and/or authors should appear here.

Electronic Supplementary Information (ESI) available: [details of any supplementary information available should be included here]. See DOI: 10.1039/x0xx00000x

employed to achieve OH⁻ conductivity in the polymer membranes for AEMFC's²⁻⁴.

The past decade has seen a significant improvement in AEMFC performance, reaching power densities as high as 0.8 - 1.4 W cm⁻², achieved utilizing polymer membranes with hydroxide conductivity ranging from 60 to 132 mS cm⁻¹, usually derived from quaternary ammonia (QA) sites on a polymer backbone⁵⁻⁷. Common factors among these results leading to high AEMFC performance are *i*) improved OH⁻ conductivity of ionomer and membrane, *ii*) the use of highly active PtRu ORR/HOR catalysts, and *iii*) the implementation of water management strategies^{2, 8}. Although significant progress has been made in the advancement of OH⁻ conductivity of anion exchange ionomers and membranes, as well as the development of PGM-Free ORR cathode materials,⁹⁻¹¹ less progress has been made in the advancement of PGM-free HOR in alkaline media. The main challenge in developing PGM-free HOR catalysts for AEMFC's lies in the different kinetic mechanism of HOR at high pH versus low pH, where the former is limited by the Volmer step of the hydrogen oxidation reaction^{12,13}. Recent understanding of the HOR mechanism in alkaline media suggests a bifunctional mechanism for HOR on bimetallic catalysts, involving the formation of H_{ad} species on a primary active site followed by the 1 e⁻ reduction of water forming OH_{ad} clusters at a secondary site^{14,15}, can facilitate the Volmer step of HOR and improve AEMFC performance using PGM-free anode materials. These findings are consistent with reports in the literature of highly active HOR catalysts in alkaline media derived from Earth-abundant materials such as carbon supported Ni, NiMo, and NiCu¹⁶⁻¹⁸.

Bimetallic systems based on Ni alloyed with base metals such as Mo, Cu, and W, have shown so far the most promise as PGM-free HOR catalysts for AEMFC's with the highest cell power density reported in the literature of ~ 120 mW cm⁻² for carbon-supported Ni₉₅Mo₅¹⁷. However, NiMo presents challenges related to performance loss due to flooding at high relative humidity, likely due to the hydrophilic nature of the catalyst pre-determined by the abundance of surface hydroxide species¹⁹⁻²¹. In the present study, we report the superior activity of a NiCu nano-alloyed HOR catalyst and its AEMFC performance. We identified a nickel-rich Ni₉₅Cu₅ nanoparticle catalyst, supported on Ketjenblack, with a true alloy structure as a candidate for a thorough *operando* micro and nano-CT to study of catalyst layer and water management during various humidified conditions (50% and 100% RH). Alloying of nickel with copper and its effects on catalyst electrochemical activity and performance in single membrane-electrode assembly (MEA) AEMFC are being discussed.

Experimental

NiCu/KB Catalyst Synthesis

NiCu/Ketjenblack was synthesized by the incipient wetness method followed by thermal reduction of nickel and copper precursors. The atomic ratio of nickel to copper was selected as

95:5 with a metal loading on Ketjenblack EC600J of 50 wt%. Necessary amounts of nickel nitrate and copper nitrate were dissolved in a minimal amount of deionized water (18 MΩ) and impregnated into the carbon support by finely mixing the slurry using a glass mortar and pestle followed by drying at T=60°C. The dried powder was then reduced in a hydrogen atmosphere (7 at%, 100 sccm) at T=550°C for 60 minutes. Once cooled, the reactor (1" I.D. quartz tube) was left for 8-12 hours under a small partial pressure of oxygen (~0.1 at%) for passivation the pyrophoric NiCu/KB catalyst. Pd/XC72R (30wt% of Pd) was used as the cathode catalyst for MEA tests and its synthesis is described elsewhere²⁰.

Catalyst Characterization

X-ray diffraction patterns were obtained using a Rigaku Smartlab diffractometer equipped with a D-Tex Ultra silicon strip detector in Bragg-Brentano focusing geometry. Cu K-α was used as the X-ray source with a K-β receiving slit filter. The catalyst was mounted on a zero-background quartz holder and scanned from 10°-140° in 2θ at a scan rate of 7°/min. MDI JADE 2010 software was used to perform whole-pattern-refinement using Ni phase data from the ICSD database as a reference [98-001-4691].

Transmission Electron Microscopy (TEM) was performed using a Joel 2010 TEMF microscope with an accelerating voltage of 200 keV. Samples were dispersed in isopropyl alcohol then sonicated for 30 minutes before being impregnated onto a carbon mesh TEM grid. Analysis of particle size and particle size distributions was performed using the ImageJ software.

XPS spectra were obtained using Kratos Axis Ultra DLD X-ray photoelectron spectrometer using a monochromatic Al Kα source operating at 125 W. All powders were conductive and mounted using conductive double-sided tape. No use of charge neutralization was necessary. Three areas for each sample were analyzed. High-resolution spectra were acquired at pass energies of 20 eV. Data analysis and quantification were performed using CasaXPS software. Sensitivity factors provided by the manufacturer were utilized. High-resolution Ni 2p and Mo 3d spectra were acquired. Ni 2p spectra were fitted using a combination of line shapes for Ni metal, NiO, Ni(OH)₂ developed by Biesinger et al.²².

Electrochemical Evaluation with Rotating Disk Electrode

HOR measurements were performed in a 3-electrode cell consisting of a glassy carbon rotating disk electrode (5 mm in diameter) as the working electrode, graphite counter electrode, and an eDAQ HydroflexTM reversible hydrogen reference electrode. Catalyst inks were prepared using 5 mg of catalyst, 150 μL of 0.5 wt% Nafion in deionized water and 850 μL isopropyl alcohol. After sonication for 30 minutes, an appropriate loading of catalyst (100 μg_{metal}, 200 μg, 300 μg_{metal}, 400 μg_{metal}, and 500 μg_{metal} total metal loading) was drop-cast onto the glassy carbon electrode and allowed to air dry. Cyclic voltammetry tests were performed in 0.1 M KOH solution saturated in N₂ or H₂. Before electrochemical

testing, the NiMo/KB catalyst was conditioned by scanning in the potential interval from -0.20 to 0.40 V at a sweep rate 100 mVs^{-1} for approximately 100 cycles in a N_2 -saturated electrolyte. All HOR measurements were performed with a sweep rate of 5 mVs^{-1} . All potentials are reported vs RHE.

From the CV data obtained in N_2 saturated electrolyte, the electrochemical surface area was calculated from the total anodic charge associated with $\text{Ni}(\text{OH})_2$ formation (0.514 mCcm^{-2}) and was normalized to the loading of metal on the working electrode. The exchange current density was then calculated from the linear polarization region of the CV performed in the H_2 saturated electrolyte, -0.01 to 0.01 V vs. RHE.

MEA Fabrication and Fuel Cell Tests

Catalyst inks for MEA fabrication were prepared by ball-milling the NiCu/KB catalyst with ionomer (Tokuyama AS4) and isopropyl alcohol at 350 r.p.m. for 30 minutes. A nominal amount of solid AS4 in catalytic layers was: anode (NiCu/KB) 45 wt% and cathode (30wt% Pt/XC72R) 30wt%. An aerosol hand-spray setup was used to deposit 4 mg cm^{-2} of the anode NiCu/KB and $0.2 \text{ mg}_{\text{Pd}} \text{ cm}^{-2}$ of the cathode Pd/XC72R catalyst onto the active surface of the 5 cm^2 membrane (Tokuyama, A201). Following the preparation of the CCM the CCM was placed in de-aerated 1M KOH for 12 hrs. This step is necessary to fully exchange Cl^- in the Tokuyama ionomer with OH^- to transfer ionomer and membrane from Cl^- into OH^- conductivity. It was then rinsed with DI water and was assembled inside of the cell hardware (FuelCellTechnology Inc, 5 cm^2) at room temperature using 4.4 Nm torque.

The cell was tested under the following conditions: H_2/O_2 , $T_{\text{cell}}=60\text{-}80^\circ\text{C}$, relative humidity (RH) of 100%, or 50%, flow rates for anode and cathode were 250 ccm and 200 ccm respectively, and with a backpressure of 20 psi_g at both the cathode and anode.

X-ray Computed Tomography

Micro X-ray CT was performed at Beamline 8.3.2 at Advanced Light Source (ALS) at Lawrence Berkeley National Laboratory (LBNL). A double-multilayer monochromator was used to select 28 keV X-rays, and detection was with a LuAG scintillator and 5x lenses with a sCMOS PCO.Edge camera, resulting in a $1.33 \mu\text{m}$ pixel dimension and a 3.3 mm horizontal field of view (FOV). For each scan, a 200 ms exposure time was used with 1025 acquired projections over a 180° rotation range. Five scans along the channel were used to observe full 1.5 lengths of the channel. 15 % overlap was used between these 5 FOVs. Single serpentine 1 mm x 1 mm channel sample holder was used for *operando* experiment. The active area of the MEA was 1 cm^2 . The operating conditions were at the OCV and cell temperature of 45°C and humidity bottles temperature of 60°C and 40°C , resulting in 58 % and 120 % RH, respectively.

Nano X-ray CT images were acquired at Beamline 32-ID at APS at Argonne National Laboratory (ANL). Energy was set at 8 keV with 1 s exposure time per projection. A Fresnel zone plate (FZP) with a 30 nm outermost zone width was used and phase ring was placed in

a back focal position to enhance soft materials contrast. 1800 back projections were acquired during the scan. An approximately $80 \mu\text{m}$ sample was cut with a micromanipulator to fit into the FOV and mounted onto a flat pin (which was then mounted onto the stage). Room RH was 50 % RH; to reach 100 % RH a droplet of water was placed onto the sample with a pin.

Image Analysis

TomoPy (open-source software developed at ANL) was used for phase retrieval and tomographic reconstructions with the Gridrec algorithm for micro-CT and the ASTRA toolbox for nano-CT²²⁻²⁵. Our earlier works provide more details on image reconstruction^{26,27}. Image segmentation and analysis were performed with Fiji/ImageJ and Avizo Fire 8.1. For nano-CT data, the image was cropped to $52 \times 48 \mu\text{m}$. The manual threshold was selected, which was the same for both 50 % RH, and 100 % RH to separate void/ionomer and solid. NiCu catalyst was easier to segment because of its brightness compared to softer carbon material. Avizo Fire 8.1 was used to align the 50 % and 100 % image stacks and ImageJ with BoneJ plug-in was used to fit pore and solid-size distributions. Volume rendering of nano-CT data was achieved with Avizo Fire 8.1.

Results and Discussion

The morphology of as synthesized NiCu/KB catalyst was investigated by TEM, where it was observed that the NiCu particles range in size from 8 nm to $> 50 \text{ nm}$ with an average particle size (τ) of 22 nm and standard deviation of 9 nm. Figure 1a shows NiCu nanoparticles well dispersed on the carbon black support. However regions of higher particle density reveal significant agglomeration and a tendency towards larger particle size. Such a broad particle distribution can be explained by a high loading of NiCu alloy on the carbon (50 wt%) and relatively high temperature reduction ($T=550^\circ\text{C}$).

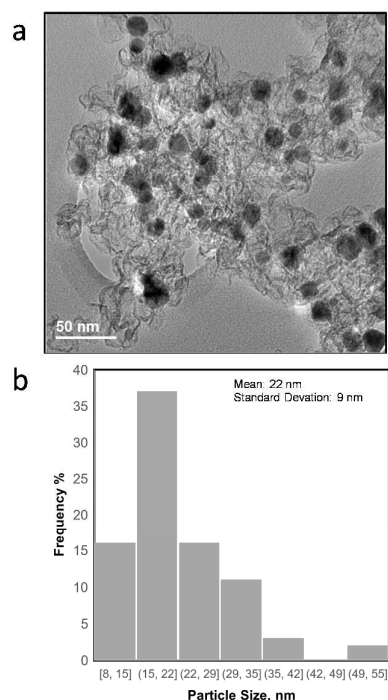


Figure 1. A) TEM image of NiCu/KB and B) particle size distribution for all NiCu particles observed in TEM micrographs.

Analysis of the X-ray diffraction pattern for NiCu/KB shows a single FCC Ni phase with a lattice constant of 3.52 Å and an average crystallite size of 27 nm, calculated from whole pattern refinement. This is in good correspondence with the TEM observations. Here, the lattice constant for a reference sample of 50 wt% Ni/KB was calculated as 3.52 Å. Applying Vegard's rule, the amount of Cu in solid solution with Ni can be calculated from the linear combination of the pure FCC lattice constants of Ni [98-001-4691] and Cu [98-001-3667], being 3.516 Å and 3.615 Å, respectively. The resulting lattice constant for a ratio of Ni to Cu of 95:5 is 3.520 Å. Due to random errors, the lattice expansion due to alloying Ni with Cu could not be measured. However, the absence of amorphous or crystalline Cu phases suggests all copper is incorporated into the FCC Ni phase presenting a true alloy at every particle size. The presence of amorphous Ni oxide and hydroxide phases is also evident in the Ni/KB XRD pattern, $\sim 37^\circ$ in 2-theta.

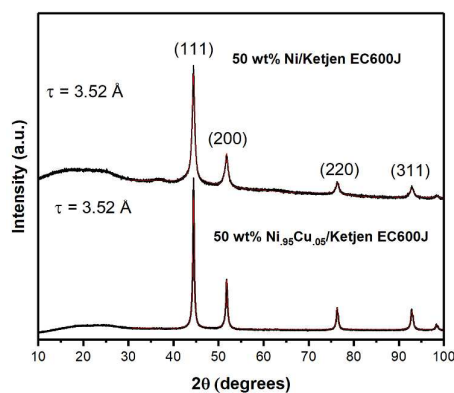


Figure 2. X-ray diffraction pattern for NiCu/KB (bottom) and Ni/KB (top) prepared by thermal reduction at $T=550^\circ\text{C}$. The peak intensities are normalized to the (111) reflection. Pattern fits are overlaid on experimental data (red).

Figure 3 shows high-resolution Ni 2p and Cu 2p photoelectron spectra obtained for Ni-KB and NiCu/KB samples. Ni 2p spectra were fitted using reference photo-peaks for metallic Ni, NiO and Ni(OH)₂ established previously.²⁸ Elemental composition and relative distribution of nickel species are shown by Figure 3c. The bimetallic sample has a smaller amount of oxygen detected, which is also reflected in the absence of hydroxides in high-resolution Ni 2p spectrum for NiCu sample. The main type of nickel in both Ni/KB and NiCu/KB samples is nickel oxide. The surface concentration of reduced metallic or alloyed Ni, however, is much larger for the alloyed sample. From high-resolution Cu 2p spectrum, it is seen that Cu is mainly present as metallic Cu with a small amount of oxides.

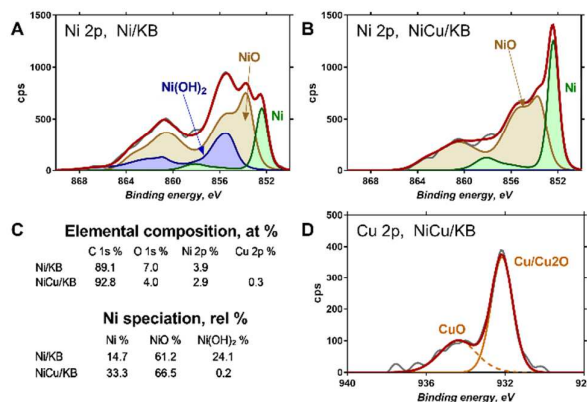


Figure 3 shows fitted (a) Ni 2p and (b) Mo 3d spectra as described in the supporting information.

Cyclic voltammetry was used to characterize the intrinsic activity towards HOR for NiCu/KB. Figure 4 summarizes the results of the electrochemical evaluation of the catalyst by cyclic voltammetry in rotating disk electrode (RDE). All voltammograms are being shown after subtraction of the capacitance current associated with Ketjenblack, as measured in 0.1 M KOH with a scan rate of 5 mVs^{-1} . Figure 4a shows a comparison of cyclic voltammograms (CV) in N₂ vs H₂ saturated electrolyte, confirming the activity of NiCu/KB towards HOR. At anodic potentials greater than 0.2 V vs. RHE, the decreasing limiting

current observed, which is due to the formation of $\text{Ni}(\text{OH})_2$, which passivates the catalyst surface and hinders HOR. This finding is consistent with previously reported observations¹⁸.

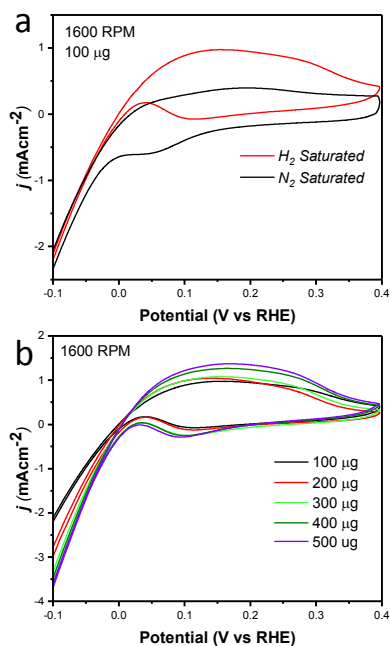


Figure 4. Cyclic voltammograms showing A) comparison of NiCu/KB in N_2 saturated 0.1M KOH (black) and in H_2 saturated 0.1M KOH and B) NiCu/KB in H_2 saturated 0.1M KOH with various metal loadings on the electrode with a sweep rate of 5 mV s^{-1} and rotation speed of 1600 rpm.

Table 1. Specific activity table of NiCu and NiMo catalysts for HOR in alkaline media.

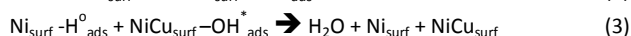
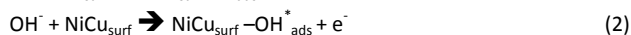
PGM-free Catalyst:	T / °C	$S \left(\frac{\text{m}^2 \text{g}^{-1}}{\text{Ni}} \right)$	$j_0 / \mu\text{A cm}^{-2} \text{ECSA}$	$i_0 / \text{A gm}^{-1}$	Reference
$\text{Ni}_{95}\text{Cu}_5/\text{Ketjenblack}$	R.T.	3.7 ± 0.2	25 ± 1	0.9 ± 0.1	This Work
$\text{Ni}_{95}\text{Cu}_5/\text{Ketjenblack}$	25	8.5	14	1.5	18
$\text{Ni}_{90}\text{Cu}_{10}/\text{Ketjenblack}$	25	10	7	1.0	18
$\text{Ni}_{95}\text{Mo}_5/\text{Ketjenblack}$	25	3.2 ± 0.4	27 ± 2	4.5 ± 0.2	17

Table 1 compares the specific activity of the catalyst reported here to the NiCu and NiMo electrocatalysts reported previously. The exchange current density normalized to the specific surface area shows strong agreement with previous studies of the NiMo system with a ratio of Ni to Mo of 95:5. Furthermore, the specific activity for NiCu in this work is 1.8 – 3.6 times higher than that of previously reported NiCu electrocatalysts by Savinova's group.¹⁸ The mass-weighted activity and specific surface area are lower than values reported previously for the NiCu system. One critical difference between this work and Savinova's work is in the fact that we have synthesized a true NiCu nanoparticle alloy, as opposed to a surface-segregated nanocomposite. One can hypothesize that in true alloy the number of Ni atoms on the surface immediately exposed to a Cu atom is larger. This should facilitate a bi-functional mechanism of HOR on true alloyed NiCu catalysts. This difference may also result from the larger average particle size of $\sim 22 \text{ nm}$, compared to $\sim 11 \text{ nm}$ in the referenced work¹⁸. By reducing particle

sizes it is possible to even further improve activities and surface area of this electrocatalyst.

Previous work reporting the high catalytic activity of $\text{Ni}_{95}\text{Cu}_5$ towards HOR in alkaline media demonstrated an electronic and ensemble effect due to alloying of Ni with Cu and the segregation of Cu islands during thermal reduction at $T=250^\circ\text{C}$ ¹⁸. At this temperature, the formation of a solid solution of Ni and Cu is not favorable, leading to phase segregation. In the present work, the synthesis was carried out at $T=550^\circ\text{C}$ and X-ray diffraction data does not suggest Ni and Cu segregation. The high activity of $\text{Ni}_{95}\text{Cu}_5$ in this work is thought to be caused purely by a chemical effect.

Recent understanding of the HOR mechanism in alkaline media on Pt^{14, 15} revealed a bifunctional mechanism consisting of *i*) the adsorption of H_{ad} intermediates on a primary active site, and *ii*) the 1 e^- reduction of water forming Pt-H_{ad} and $\text{OH}_{\text{q-aq}}$, thus facilitating the Volmer step in the HOR mechanism. It was suggested that a strategy for lowering the overpotential for HOR in alkaline media could involve alloying Pt, or the primary active metal site, with a base metal, which forms a passivated hydroxide layer. In doing so, the Volmer step of the reaction may be facilitated, as it involves the approach of intermediate OH^- through the outer Helmholtz plane towards a negatively charged electrode, which is unfavorable for negatively charged species. In the present work, Ni is considered as the primary active site for the generation of H_{ad} while Cu acts as a base metal which may form a hydroxide passivation layer. As surface analysis had shown, Ni surface in Ni/KB catalysts sample has a passivated hydroxide layer as an "overcoat", which makes it not favorable for initial hydrogen adsorption. In contrast, in alloyed NiCu/KB catalyst sample, the analysis shows Ni surface free of hydroxides, and thus exposed Ni surface could serve as primary sites for the first step of the reaction, while Cu acts as a second step of water forming Ni-H_{ad} and $\text{NiCu-OH}_{\text{q-aq}}$. (see Figure 5). We hypothesize here that NiCu fully alloyed nanoparticle catalyst supports a bi-functional Tafel-Volmer mechanism for hydrogen oxidation in alkaline electrolyte,¹³ which outlined for this specific materials selection in equations 1-3:



This suggested mechanism largely agrees with those proposed for PGM metal catalyst (such as Pd), which are alloyed with a transition metal (e.g. Ni). The observations allow us to draw analogy between the NiCu alloyed nano-particle catalysts and PdNi in their HOR reactivity and mechanism.³³

Additionally, the effect of catalyst layer thickness was further examined by comparing the specific activity and mass-weighted activity at each catalyst loading (Figure S2). A trend of decreasing specific activity as well as mass-weighted activity was evident and is consistent with the less than proportional increase in current

density with increased catalyst loading (Figure 4b). As the exchange current density calculated from the micro-polarization region is not influenced by mass transfer characteristics of the electrode, it seems evident that an increase in catalyst layer thickness results in an increase in electrochemical impedance. Reaction impedance associated with the Volmer step of the HOR mechanism, the formation of intermediate and surface OH^- , can then explain why $\text{Ni}_{95}\text{Cu}_5$ performance in both RDE and MEA methods does not reach that of PGM catalysts. This factor also highlights a critical design point in optimizing the catalyst layer in MEA and fuel cell tests.

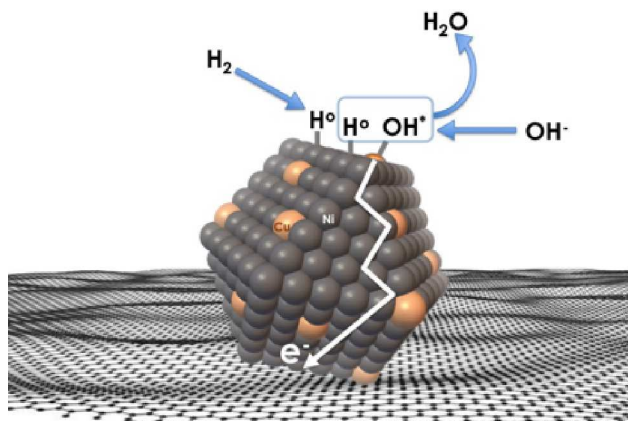


Figure 5. Conceptual schematic of the mechanism of HOR on alloyed NiCu nanoparticle, supported on a carbonaceous surface.

These results, in combination with our previous results obtained for NiMo/KB for HOR in alkaline media²⁹, suggest the affinity of the alloying base metal to hydroxyl adsorption to be in an optimal range (not be too strong, nor too weak) in order to facilitate both abundance of surface hydroxyl groups available in proximity to atomically adsorbed hydrogen for water formation, and subsequent water release. This concept should be further verified and studied in detail by the DFT and other modelling tools.

MEA Fuel Cell Tests

MEA studies were performed using the catalyst coated membrane (CCM) method of MEA fabrication with Tokuyama membranes and ionomers. CCM method was selected due to the poor thermal stability of the Tokuyama membrane and ionomer at temperatures above 80°C, typically used for hot-pressed MEA gas-diffusion electrode (GDE) method of fabrication. The poor stability of AEM ionomers at elevated temperature is due to the susceptibility of the quaternary ammonia sites in the crosslinked polymer to nucleophilic attack by OH^- .

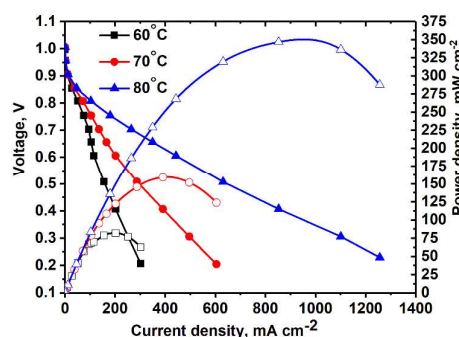


Figure 6. Polarization curve (no IR-corrections) of MEA with NiCu/KB anode. Conditions: $T_{\text{cell}}=60, 70$ and 80°C , $\text{RH}=100\%$, H_2 and O_2 backpressure = 20 psig, Anode: NiCu/KB, 4 mgcm^{-2} , Cathode: Pd/XC72R, 0.2 mgcm^{-2} [p.d]

Steady-state polarization curves (see Figure 6) were obtained at various temperatures under fully humidified conditions producing a peak power density of $\sim 350 \text{ mWcm}^{-2}$ at 80°C . Decreasing RH did not result in higher current densities, as was observed for NiMo electrocatalyst in the previous study²⁹. This is indicative that in this anode catalyst layer, water management is more efficient. For three temperatures the OCV achieved was high – above 1.0 V. As the temperature was raised, due to faster reaction kinetics the current density increased, particularly in the activation region. Ohmic and mass-transport current densities also improved at higher temperatures due to improved OH^- conductivity and improved water removal by evaporation and phase-change induced flow³⁰. The peak power density obtained is, at present, the highest reported for any PGM-free anodic material integrated as HOR catalyst in an AEM fuel cell tested as MEA.

Micro X-ray CT

Figure 7a and b show a three-dimensional representation of grey-scale tomography data for the cell with 58 % and 120 % RH feeds and OCV condition. The anode NiCu/KB catalyst layer is the thickest (140 μm) and brightest part within the cell. For a PGM-free CCM 140 μm is a moderate thickness. The catalyst layer is observed to be densely packed, crack-less and fairly uniform in thickness. Cathode catalyst layer showed some mud cracks. Comparison of data at 58 and 120 % RH reveals no apparent micro-scale swelling and no liquid condensation. In our earlier work, we showed that NiMo/KB act hydroscopically – absorbing large amounts of water²⁹. In that study polarization behavior was strongly depended on RH, where the peak power density was reached at 70 % RH. Here, water flooding is not an issue at 100 % RH, as observed by both polarization data and X-ray CT images. Areas of high local hydrophilicity found in our previous study are possibly due to the secondary phase of Mo, or be due to the chemical state of Ni. Opposite wettability behavior was found in a recent study of model electrodes and in theory, suggesting that $\beta\text{-Ni}(\text{OH})_2$ is hydrophobic, whereas $\beta\text{-NiOOH}$ (001) is hydrophilic^{18, 19}. These changes in wettability were ascribed to changes in chemical composition of the surface.

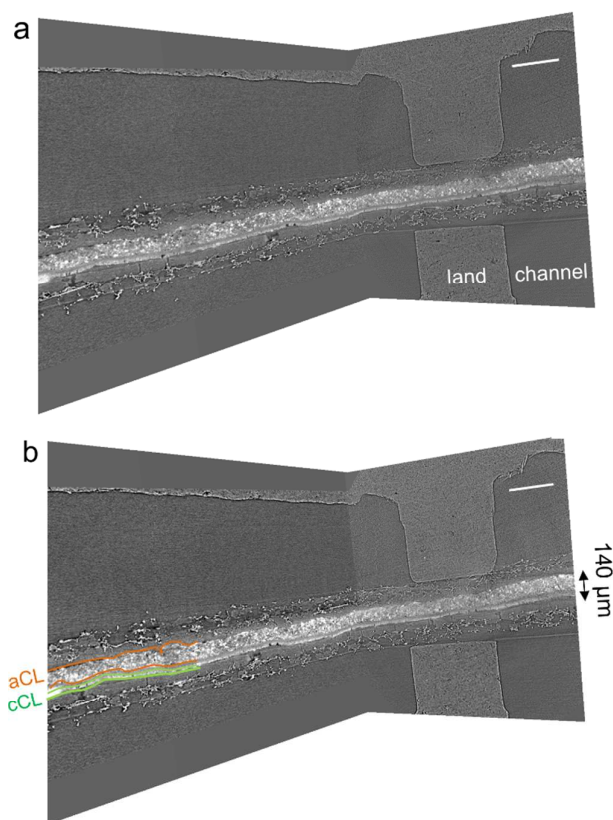


Figure 7. Micro-CT representation of the MEA within operando hardware for a) 58 % and b) 120 % RH at a temperature of 45°C. The scale-bar is 500 μm.

Nano X-ray CT

No apparent difference between 58 and 120 % RH was observed from the micro X-ray CT data for larger macropores (> 1 μm). To probe water distribution in smaller macropores (<1 μm), we utilize nano X-ray CT imaging. Figure 8 shows three-dimensional NiCu distribution within carbon black. Average carbon agglomerate radii were 0.55 μm with unimodal distribution. At the same time, NiCu catalyst had a wider distribution of sizes. From micro X-ray CT in Figure 7, NiCu distribution on a micro-scale is uniform. Within 52 μm of the nano-CT domain probed, the NiCu average cluster size was found to be 1.23 μm. Furthermore, NiCu occupies 8 % of the electrode volume, as shown in Figure 8f, where the remaining of the volume is either carbon support or void space.

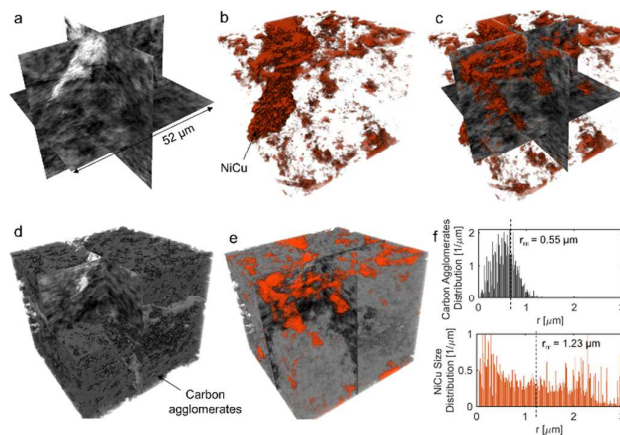


Figure 8. Three-dimensional representation of NiCu/KB electrode, with a,) grey-scale, b) volume-rendered NiCu (shown in red), c) overlaying a and b, d) carbon agglomerates segmented, e) overlaying d and b. The carbon agglomerate distribution and NiCu size distribution are shown by f.

Figure 9 shows a comparison of void/ionomer distribution between 50 % and 100 % RH conditions. The difference between these identical location nano X-ray CTs is subtle. However, the darker domains expand when water is introduced into the sample. Darker domains correspond to both void and ionomer spaces. Figure 9c and d show the locations where ionomer expanded to and its schematic, respectively. The volume fraction of void/ionomer space increased from 12 to 17 % as RH increased from 50 to 100 %.

Volume-rendered void/ionomer space is shown in Figure for both RHs. From the size distribution, the mean radius of voids at 50 % RH is 0.36 μm, whereas for 100 % RH it is larger- being 0.43 μm. From subtracting the two void/ionomer distributions, it is apparent that ionomer swells uniformly from smaller to larger voids. The critical pore radius where this transition happened is 0.6 μm.

From the water-management perspective, if we assume a uniform surface tension corresponding to a more hydrophobic nature of the material, having water in larger macropores is advantageous. Large macropores present lower-resistance pathways for water removal into the gas-flow channel avoiding local flooding. Comparing this study to our previous one²⁹ it is evident that surface properties of the electrocatalysts themselves dictate the local wettability, as carbon support used in these two studies was identical. Hence, the effective MEA design requires more homogeneous catalyst dispersion, low thickness and hierarchical morphology but also understanding of surface chemistry and its effect on local wettability, which has not been discussed in literature. X-ray CT observations reported here on NiCu/KB catalyst layer are in contrast with our previous findings when NiMo/KB catalyst was used.²⁹ One can speculate that more oxophilic character of Mo moieties provides a favourable local micro-environment for water nucleation and thus results in prominent liquid water formation in the anode catalyst layer, observed as “flooding” in NiMo catalysts. Such behaviour can be expected across the sub-category of bi-metallic³² or composite³⁴ HOR catalysts, employing oxophilic moieties as co-catalysts.

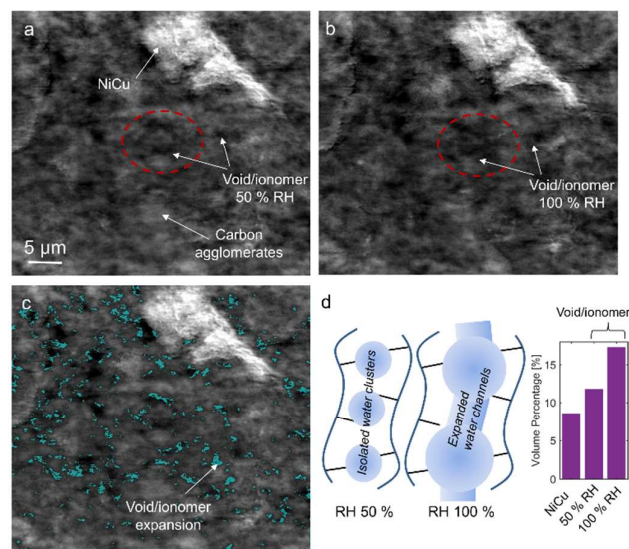


Figure 9. Nano X-ray CT cross-section tomographs of a) 50 % RH and b) 100 % RH, where carbon agglomerates, void/ionomer space, and NiCu are marked. C) The difference in void/ionomer space after subtracting a from b. d) A schematic of ionomer swelling and volume percentage for NiCu, and void/ionomer at two RHs.

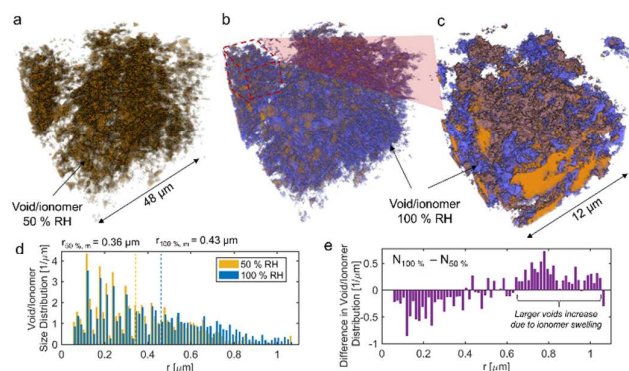


Figure 10. Volume-rendered void/ionomer space for a) 50 % RH, and b) combined 50 % and 100 % and the difference between 100 % and 50 %, c) zoom-in into 12 μm of the FOV. The void/ionomer size distributions, as well, as mean radii are shown in d. The difference between 100 % and 50 % between void/ionomer is shown by e.

Conclusions

NiCu fully alloyed nanoparticles, supported on medium surface area mesoporous carbon black (Ketjenblack) are described here as a new, scalable and practical HOR catalyst suitable for integration in a practical AMFC anode. Structure-to-property relationship studies reveal a bi-functional mechanism of HOR on NiCu catalyst, with atomically dispersed Cu moiety playing substantial role in the balancing surface hydroxyl availability and forming and releasing water as a reaction product. Consequently, this new catalyst demonstrates superior area specific activity in RDE and record-setting power density for PGM-free AMFC anode approaching 350 mWcm⁻² at 80°C.

NNano and micro X-ray CT results suggest that the nickel state in NiCu is hydrophobic in nature, where the NiCu surface may be

isostructural with β -Ni(OH)₂. The improved water distribution supports this conclusion observed *in operando* for NiCu/KB compared to NiMo/KB, resulting in improved water management in the MEA for NiCu/KB.

Acknowledgements

The project is supported by DOE EERE program, Incubator Award DE-EE0006962 “Development of PGM-free Catalysts for Hydrogen Oxidation Reaction in Alkaline Media”. This research used resources of the Advanced Photon Source, a U.S. Department of Energy (DOE) Office of Science User Facility operated for the DOE Office of Science by Argonne National Laboratory under Contract No. DE-AC02-06CH11357. The Advanced Light Source is supported by the Director, Office of Science, Office of Basic Energy Sciences, of the U.S. Department of Energy under Contract No. DE-AC02-05CH11231.

All authors declare no conflict of interest.

References

1. J. R. Varcoe, P. Atanassov, D. R. Dekel, A. M. Herring, M. A. Hickner, P. A. Kohl, A. R. Kucernak, W. E. Mustain, K. Nijmeijer, K. Scott, T. Xu and L. Zhuang, *Energy & Environmental Science*, 2014, **7**, 3135-3191.
2. D. R. Dekel, *Journal of Power Sources*, 2018, **375**, 158-169.
3. G. Merle, M. Wessling and K. Nijmeijer, *Journal of Membrane Science*, 2011, **377**, 1-35.
4. S. Maurya, S.-H. Shin, Y. Kim and S.-H. Moon, *RSC Advances*, 2015, **5**, 37206-37230.
5. R. B. Kaspar, M. P. Letterio, J. A. Wittkopf, K. Gong, S. Gu and Y. S. Yan, *J. Electrochem. Soc.*, 2015, **162**, F483-F488.
6. Y. Wang, G. Wang, G. Li, B. Huang, J. Pan, Q. Liu, J. Han, L. Xiao, J. Lu and L. Zhuang, *Energy & Environmental Science*, 2015, **8**, 177-181.
7. R. C. T. Slade, J. P. Kizewski, S. D. Poynton, R. Zeng and J. R. Varcoe, in *Fuel Cells: Selected Entries from the Encyclopedia of Sustainability Science and Technology*, ed. K.-D. Kreuer, Springer New York, New York, NY, 2013, DOI: 10.1007/978-1-4614-5785-5_2, pp. 9-29.
8. A. Serov, I. V. Zenyuk, C. G. Arges and M. Chatenet, *Journal of Power Sources*, 2018, **375**, 149-157.
9. E. F. Holby, G. Wu, P. Zelenay and C. D. Taylor, *The Journal of Physical Chemistry C*, 2014, **118**, 14388-14393.
10. A. Morozan and F. Jaouen, *Energy & Environmental Science*, 2012, **5**, 9269-9290.
11. K. Strickland, E. Miner, Q. Jia, U. Tylus, N. Ramaswamy, W. Liang, M.-T. Sougrati, F. Jaouen and S. Mukerjee, *Nat. Commun.*, 2015, **6**, 7343.
12. J. Durst, A. Siebel, C. Simon, F. Hasche, J. Herranz and H. A. Gasteiger, *Energy & Environmental Science*, 2014, **7**, 2255-2260.
13. B.E. Conway, B.V. Tilak, *Electrochimica Acta*, 2002, **47**, 3571-359413.
14. J. Li, S. Ghoshal, M. K. Bates, T. E. Miller, V. Davies, E. Stavitski, K. Attenkofer, S. Mukerjee, Z.-F. Ma and Q. Jia,

- Angewandte Chemie International Edition*, 2017, **56**, 15594-15598.
15. N. Ramaswamy, S. Ghoshal, M. K. Bates, Q. Jia, J. Li and S. Mukerjee, *Nano Energy*, 2017, **41**, 765-771.
16. Z. Zhuang, S. A. Giles, J. Zheng, G. R. Jenness, S. Caratzoulas, D. G. Vlachos and Y. Yan, *Nat. Commun.*, 2016, **7**, 10141.
17. S. Kabir, K. Lemire, K. Artyushkova, A. Roy, M. Odgaard, D. Schlueter, A. Oshchepkov, A. Bonnefont, E. Savinova, D. C. Sabarirajan, P. Mandal, E. J. Crumlin, I. Zenyuk, P. Atanassov and A. Serov, *Journal of Materials Chemistry A*, 2017, **5**, 24433-24443.
18. A. G. Oshchepkov, P. A. Simonov, O. V. Cherstiouk, R. R. Nazmutdinov, D. V. Glukhov, V. I. Zaikovskii, T. Y. Kardash, R. I. Kvon, A. Bonnefont, A. N. Simonov, V. N. Parmon and E. R. Savinova, *Topics in Catalysis*, 2015, **58**, 1181-1192.
19. Y.-H. Chang, N. Y. Hau, C. Liu, Y.-T. Huang, C.-C. Li, K. Shih and S.-P. Feng, *Nanoscale*, 2014, **6**, 15309-15315.
20. M. J. Eslamibidgoli, Gro and M. Eikerling, *Physical Chemistry Chemical Physics*, 2017, **19**, 22659-22669.
21. A. Serov, N. I. Andersen, S. A. Kabir, A. Roy, T. Asset, M. Chatenet, F. Maillard and P. Atanassov, *J. Electrochem. Soc.*, 2015, **162**, F1305-F1309.
22. M. C. Biesinger, B. P. Payne, L. W. M. Lau, A. Gerson and R. S. C. Smart, *Surface and Interface Analysis*, 2009, **41**, 324-332.
23. D. Gürsoy, F. De Carlo, X. Xiao and C. Jacobsen, *Journal of Synchrotron Radiation*, 2014, **21**, 1188-1193.
24. D. M. Pelt, D. Gürsoy, W. J. Palenstijn, J. Sijbers, F. De Carlo and K. J. Batenburg, *Journal of synchrotron radiation*, 2016, **23**, 842-849.
25. F. De Carlo, D. Gürsoy, F. Marone, M. Rivers, D. Y. Parkinson, F. Khan, N. Schwarz, D. J. Vine, S. Vogt and S.-C. Gleber, *Journal of Synchrotron Radiation*, 2014, **21**, 1224-1230.
26. V. De Andrade, A. Deriy, M. J. Wojcik, D. Gürsoy, D. Shu, K. Fezzaa and F. De Carlo.
27. I. V. Zenyuk, D. Y. Parkinson, L. G. Connolly and A. Z. Weber, *Journal of Power Sources*, 2016, **328**, 364-376.
28. T. Asset, A. Roy, T. Sakamoto, M. Padilla, I. Matanovic, K. Artyushkova, A. Serov, F. Maillard, M. Chatenet, K. Asazawa, H. Tanaka and P. Atanassov, *Electrochim. Acta*, 2016, **215**, 420-426.
29. S. Kabir, K. Lemire, K. Artyushkova, A. Roy, M. Odgaard, D. Schlueter, A. Oshchepkov, A. Bonnefont, E. Savinova, D. C. Sabarirajan, P. Mandal, E. J. Crumlin, I. V. Zenyuk, P. Atanassov and A. Serov, *Journal of Materials Chemistry A*, **under review**.
30. S. Kabir, K. Lemire, K. Artyushkova, A. Roy, M. Odgaard, D. Schlueter, A. Oshchepkov, A. Bonnefont, E. Savinova, D. C. Sabarirajan, P. Mandal, E. J. Crumlin, I. Zenyuk, P. Atanassov and A. Serov, *Journal of Materials Chemistry A*, 2017, DOI: 10.1039/C7TA08718G.
31. A. D. Shum, D. Y. Parkinson, X. Xiao, A. Z. Weber, O. S. Burheim and I. V. Zenyuk, *Electrochimica Acta*, 2017, **256**, 279-290.
32. M.H. Tang, C. Hahn, A.J. Klobuchar, J.W. Desmond Ng, J. Wellendorff, T. Bligaard, T. Jaramillo, *Phys. Chem. Chem. Phys.*, 2014, **16**, 19250-19257
33. M. Alesker, M. Page, M. Shviro, Y. Paska, G. Gershinsky, D.R. Dekel, D. Zitoun, *J. Power Sources*, 2016, **304**, 332-339
34. H.A. Miller, F. Vizza, M. Marelli, A. Zadick, L. Dubau, M. Chatenet, S. Geiger, S. Cherevko, H. Doan, R.K. Pavlicek, S. Mukerjee, D.R. Dekel, *Nano Energy*, 2017, **33**, 293-305